IOP PUBLISHING JOURNAL OF GEOPHYSICS AND ENGINEERING

J. Geophys. Eng. **6** (2009) 1–20 doi:10.1088/1742-2132/6/1/001

Comparative tests on different multi-electrode arrays using models in near-surface geophysics

R Martorana[1], G Fiandaca[1], A Casas Ponsati[2] and P L Cosentino[1]

[1] Dipartimento di Chimica e Fisica della Terra, Università di Palermo, via Archirafi 26, 90123 Palermo, Italy

[2] Departament de Geoquímica, Petrologia i Prospecció Geològica, Universitat de Barcelona, Facultat de Geologia c/Martí i Franquès, s/n 08028 Barcelona, Spain

E-mail: r.martorana@unipa.it, gianluca.fiandaca@unipa.it, albert.casas@ub.edu and pietro.cosentino@unipa.it

Received 31 March 2008
Accepted for publication 11 November 2008
Published 12 December 2008
Online at stacks.iop.org/JGE/6/1

Abstract

In this paper, the response of different synthetic models to geoelectrical multi-electrode surveys is studied. The models considered are related to two main problems, which are very common in geophysical research regarding hydrogeology and engineering. The first class of models represents buried walls, similar archaeological remains or remains of buried foundations; the other class corresponds to a sea-water intrusion of a fresh water aquifer, which is generally studied in hydrogeophysics. A set of 2D simulations, starting from the synthetic models, was carried out to compare the behaviour of the different arrays when acquiring measurements of electrical resistivity tomography. For each model, the apparent resistivity data—and relative pseudo-sections—were calculated for common electrode arrays (Wenner, dipole–dipole, Wenner–Schlumberger). Furthermore, a 'non-classical' configuration (i.e. the linear grid) was also tested. The synthetic data, after adding different levels of Gaussian noise, were inverted using RES2DINV software; then the interpretative models were compared with the initial synthetic models using different parameters to estimate the quality of the matching. Finally, the comparison between the results obtained using the various arrays is presented. Furthermore, the effectiveness of the various arrays is evaluated for each problem, also taking into account some other characteristics of the arrays, including the associated practical advantages in time consumption and noise level. Results on synthetic data were also confirmed by two field tests: one at an archaeological site survey and one at a coastal aquifer study.

Keywords: linear grid, dipole–dipole, Wenner, Wenner–Schlumberger, buried wall, sea intrusion wedge

1. Introduction

Modelling is a very useful tool in applied geophysics for comparing the resolution power of different dc resistivity electrode arrays. In electrical resistivity tomography (ERT), an electrical field can be applied to the subsoil in a lot of different ways. In fact, different electrode arrays are used to carry out ERT measurements.

'Classical' arrays, such as pole–pole, Wenner, Wenner–Schlumberger, pole–dipole and dipole–dipole, are frequently employed in 2D or 3D resistivity imaging applications (Dahlin 1996, Storz *et al* 2000).

The choice of a particular array in ERT can make a substantial difference to the results, also depending on the geometry and resistivity of the investigated structures. The principal differences in the results are associated with

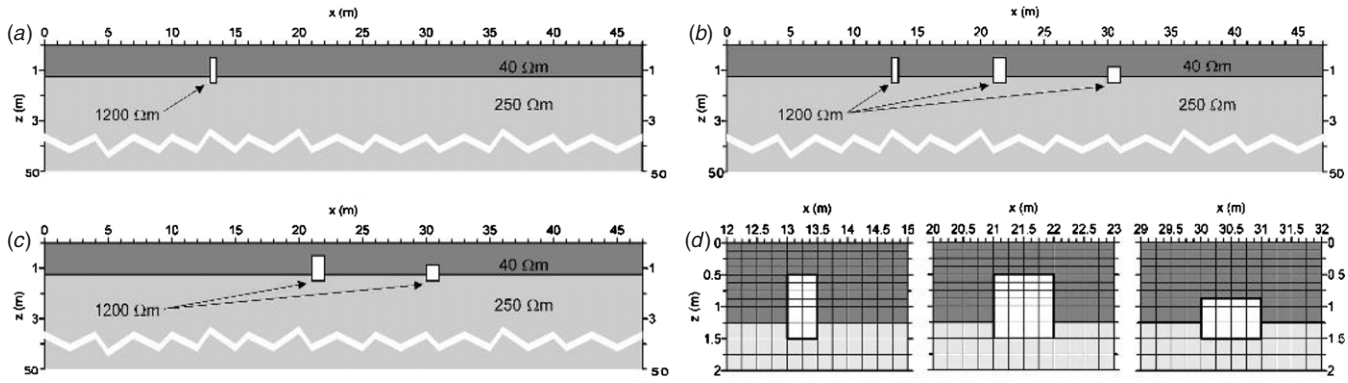

Figure 1. (*a*) Model of one resistive buried wall (1 m high and 0.5 m wide) founded on a less resistive basement and covered by a conductive overburden. (*b*) Model of two resistive buried walls. The wall on the left is 1 m high and 1 m wide, and that on the right is 0.62 m high and 1 m wide. (*c*) Model of three resistive buried walls. The wall on the left is 1 m high and 0.5 m wide, the wall in the middle is 1 m high and 1 m wide, and that on the right is 0.62 m high and 1 m wide. (*d*) Enlarged images of the models near the walls in figure 1(*c*), showing the chosen size of the blocks.

the resolution power, the production of ghost anomalies in the images not related to physical anomalies, as well as the large deviations from the true-model resistivity. The resolution of an electrode array is strongly influenced by the sensitivity pattern, which is very different for each array. Many studies have been carried out recently to compare the advantages and limits of the most common arrays that give resistivity images. Park and Van (1991) and Van *et al* (1991) stressed the difficulty of acquiring noiseless data in the field using pole–pole arrays. Sasaki (1992) compared the resolution of cross-hole resistivity tomography using pole–pole, pole–dipole and dipole–dipole arrays, and established that a dipole–dipole array is more suitable for resolving complex structures. By comparing the previous arrays, Oldenburg and Li (1999) stressed the differences in depth of investigation of each array in terms of the inverted models. Studies on the imaging resolution and on the reliability of the Wenner array (Dahlin and Loke 1998, Olayinka and Yaramanci 2000) stressed the importance of the sampling density in determining the resolution of this configuration.

In the last 10 years, developments in microelectronics have brought great improvements to both data acquisition systems and inversion software. Consequently, resistivity tomographic techniques have achieved important improvements. Recent studies (Daily and Owen 1991, Park and Van 1991, Shima 1992, Li and Oldenburg 1992, Sasaki 1994, Loke and Barker 1995, 1996, LaBrecque *et al* 1996, Dahlin and Zhou 2004) have shown that by using a large set of well-distributed and spaced measurements, it is generally possible to obtain relatively accurate 2D or 3D resistivity images of the subsurface.

Recently, multi-channel data acquisition systems have made it possible for researchers to make use of unconventional electrode array configurations, in addition to the 'classical' arrays, thereby enabling many simultaneous measurements to be taken for each injection point, thus significantly reducing time for data acquisition. Examples of these kinds of arrays are the *moving gradient* array and the *midpoint-potential-referred* array. These arrays were already successfully applied by the former USSR (e.g. Veshev 1965), and their high efficiency was shown (e.g. Khesin 1969). Dahlin and Zhou (2004) performed various numerical simulations to compare the resolution and efficiency of resistivity imaging surveys for ten different electrode arrays: pole–pole, pole–dipole, half-Wenner, Wenner, Schlumberger, dipole–dipole, Wenner-β, γ-array, moving gradient and midpoint-potential-referred measurement arrays. They recommend the moving gradient, pole–dipole, dipole–dipole and Schlumberger arrays, rather than the others, for resistivity imaging, although the final choice should be determined by the type of geology expected, the purpose of the survey and logistical considerations.

In this work, a multi-polar array, called a linear grid (Fiandaca *et al* 2005, Capizzi *et al* 2007) optimized for multi-channel acquisition, is tested, compared with other well-known arrays (Wenner, Wenner–Schlumberger and dipole–dipole) and discussed.

Simulations with the above-mentioned arrays have been carried out on different 2D models, which represent common studies of coastal hydrogeology (a sea-intrusion wedge), engineering practices (buried foundations) and archaeological research (buried walls or similar remains). The models have been designed with features (i.e. geometry and resistivity contrasts) for which it is not easy to retrieve the underground structures. However, in point of fact these models agree quite well with the typical conditions of field work carried out in archaeology, foundations and hydrogeology research.

The first 2D model (figure 1(*a*)) simulates a buried electrically resistive wall overlain on a less resistive bed and covered by a conductive layer. The chosen electrode spacing was twice the width of the wall: in this way, the errors would be large. Figure 1(*b*) shows a slightly different model containing two buried walls with different dimensions and positions in the model; figure 1(*c*) presents the model obtained by the integration of the previous two models. Furthermore, starting from the model of figure 1(*a*), other simulations were done by varying the resistivity contrast between the wall and the overburden and the thickness of the overburden.

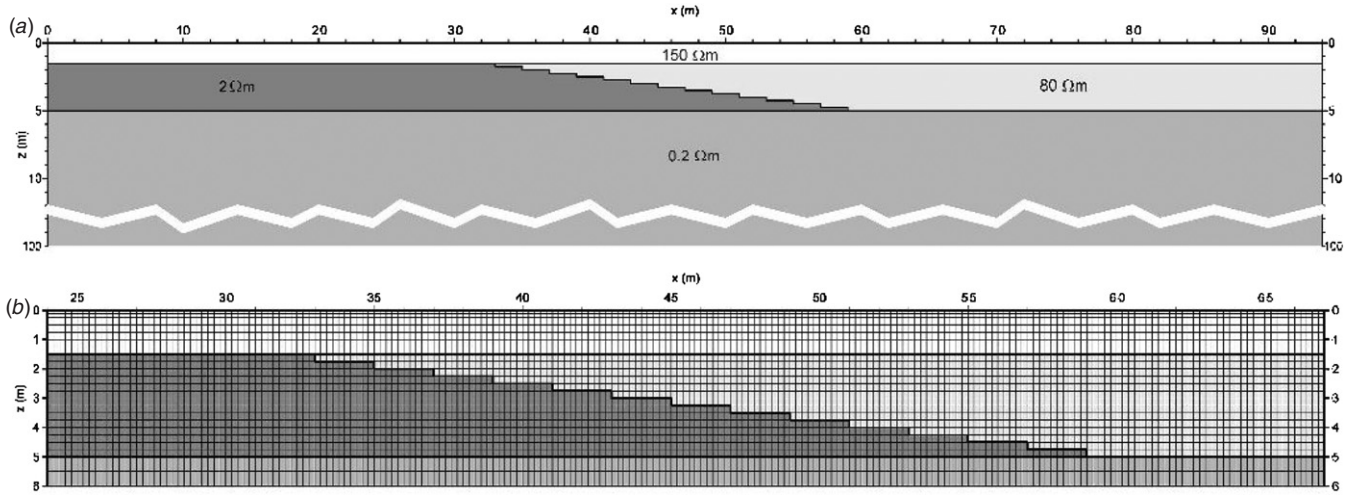

Figure 2. (*a*) Model of an aquifer characterized by a sea wedge intrusion. The salt-water zone passes into the fresh-water zone laterally; the water area is covered by a resistive overburden and lies on a conductive basement. (*b*) A zoomed image of the model in figure 2(*a*) that refers to the lateral variation of the resistivity, showing the chosen size of the blocks.

A different 2D model (figure 2) simulates an aquifer partially intruded by sea water. Typical cases of salt-water intrusion in coastal aquifers have been successfully studied using different geoelectrical techniques. These include the dc resistivity method (Patra 1967, Hagemeyer and Stewart 1990), profiling electromagnetic (EM) method (Stewart 1982), transient electromagnetic (TEM) method (Mills *et al* 1988, Hoekstra and Blohm 1990, Goldman *et al* 1991), induced polarization (IP) method (Khesin 2001) and combined application of dc and TEM methods (Yang *et al* 1999). Furthermore, combined applications of geoelectrical and seismic techniques were also used (Deidda *et al* 2006, Cosentino *et al* 2007).

The model of salt-water intrusion discussed in this work is designed to include a low-resistivity basement (e.g. clay) under the aquifer. This latter is characterized by a higher resistivity value in the fresh water zone, in respect of the intruded zone.

Several tests were done with the purpose of establishing the spatial resolution and the noise sensitivity of each different array for both models.

2. Outline

The steps involved in the simulations and the subsequent assessment of the quality of the inversions are summarized as follows.

2.1. Forward modelling

Models are subdivided into a number of rectangular blocks (pixels of the forward models), arranged to highlight the changes in resistivity and to allow reliable estimates of the voltage values in high voltage gradient regions.

The calculation of the apparent resistivity data, of use in constructing pseudo-sections, was carried out by forward modelling using RES2DMOD (Loke 2002), which includes a finite-element approach to calculate the potential distribution due to point current sources. The potential distribution was then converted into apparent resistivity values. Surveys with 48 electrodes, spaced 1 m, were simulated using different arrays. The mesh comprised four nodes per unit electrode spacing. Noise was added to the synthetic data by random values generated with Gaussian distribution (i.e. with the mean value equal to zero and the standard deviation equal to 2% and 5% of the unperturbed resistivity values).

These data sets were used as input for 2D inversions.

2.2. Inversion of data

Software RES2DINV version 3.53e (Loke and Barker 1996), which is based on the smoothness-constrained, nonlinear least-squares optimization technique, was used to obtain the interpretative model.

The inversion algorithm is an iteratively reweighted least-squared method based on the Gauss–Newton method; in addition, the Jacobian matrix of partial derivatives is always recalculated using the finite-element method.

The first step in the inversion is the estimation of an initial model. Next, the solution is iteratively improved by varying the model parameters to minimize the discrepancies between the observed and the calculated responses.

The inversion program uses a 2D model divided into a number of rectangular blocks (pixels of inversion models), whose arrangement is made according to the distribution of the data points in the pseudo-section.

We chose to prevent the main horizontal discontinuities (i.e. layer boundaries) of the models from corresponding to the limits of the pixels used in the inversion models, as generally happens in real cases, when the actual model is unknown. This choice practically imposes discrepancies in retrieving the thicknesses of the layers.

The inversions were performed for noise-free data as well as for the same data containing 2% and 5% Gaussian noise. In order to be able to compare the results obtained from the

Table 1. Values of the main parameters chosen for all the inversions.

Inversion settings	
Finite-element method	
Initial damping factor	0.30
Minimum damping factor	0.03
Number of nodes between adjacent electrodes	4
Increase of the damping factor with depth	1.05
Robust data constraint used: cut-off value	0.05
Robust model constraint used: cut-off value	0.005
Blocks have the same width as the electrode step	
RMS convergence limit	1%
Percentage RMS error for convergence	1%
Line search RMS change limit	0.4%
Logarithm of apparent resistivity used	
Reference resistivity used is the average value	
Gauss–Newton optimization method	

different arrays, it was decided to fix the values of the inversion parameters for all the inversions. These parameters are shown in table 1.

Olayinka and Yaramanci (2000) note that Res2Dinv software stops the improvement of the fitting after only a few iterations, with additional iterations worsening the typical match with the synthetic model; for this reason we verified that, using the software setting of table 1, the quality of the inversions improved after each iteration.

2.3. Calculation of the model misfit on synthetic data

The interpretative models were compared with the synthetic models using two misfit parameters to estimate the quality of the matching.

In the inversions discussed in this work, the subdivisions in blocks of inverted models do not correspond to those of the equivalent synthetic models. For this reason, in order to evaluate the resistivity mismatch between inverted and synthetic models, a new refined mesh was designed for the comparison for each inversion. These refined meshes were obtained from the superposition of the boundaries of all the blocks of the inverted and the synthetic models.

The first misfit parameter is defined as follows:

$$F_{i,j}^{2D} = \lg\left(\frac{\rho_{\mathrm{Inv}}^{i,j}}{\rho_{\mathrm{Mod}}^{i,j}}\right), \tag{1}$$

where $\rho_{\mathrm{Mod}}^{i,j}$ and $\rho_{\mathrm{Inv}}^{i,j}$ are the resistivity of the original model and that of the inverted model respectively, for the *j*th column of the *i*th row of the refined mesh.

The main features of this misfit parameter are the following:

(1) it gives a relative misfit, independent of the value of the model resistivity;
(2) positive values of the parameter imply an overestimation of the resistivity and vice versa;
(3) it basically considers the order of magnitude of the discrepancies.

Another interesting parameter that gives appreciable information, especially about the pattern recognition of the layers of different resistivities, is defined as the average of F^{2D}, as follows:

$$F_i^{1D} = \frac{\sum_{j=1}^{N_i} \lg\left|\frac{\rho_{\mathrm{Inv}}^{i,j}}{\rho_{\mathrm{Mod}}^{i,j}}\right|}{N_i} \tag{2}$$

calculated over each row of the refined mesh. N_i is the number of pixels of the *i*th horizontal row.

Equations (1) and (2) define quantitative criteria to evaluate differences between quantities of information obtained on the inverted model with respect to the synthetic model (Khesin *et al* 1996). These two parameters are useful for a recognition of the mismatching areas; nevertheless, regarding the quantitative discrepancies at the boundaries between zones with different resistivities, the values of the misfit parameters are strongly affected by the resistivity contrasts.

3. Arrays

In this work, apparent resistivity pseudo-sections were calculated for the most common electrode arrays so as to produce rough 2D resistivity images. The 'classical' arrays chosen were Wenner (hereafter W), dipole–dipole (hereafter DD) and Wenner–Schlumberger (hereafter WS). Furthermore, a new 'multi-electrode' configuration, called a linear grid (hereafter LG), was tested.

A multi-electrode cable with fixed inter-electrode spacing is often used in the acquisition of electrical data for tomographic images. Different sets of measurements can be acquired with this system by using different electrode arrays. These can be obtained by increasing both the electrode step (i.e. the distance between potential electrodes) and the *n* factor (i.e. the ratio of the distance of the B–M electrodes to the M–N dipole spacing, where A and B are the current electrodes, and M and N are the potential electrodes). Generally, the electrode step is a multiple of the electrode spacing (*a*), that is, the minimum electrode distance.

In principle, it is possible to obtain a high-resolution image by acquiring a data set using only one type of array (i.e. by changing the centre point of the array as well as the values of *a* and/or *n*). On the other hand, we should also bear in mind the fact that a large number of point data can increase both the acquisition time and the noise contamination (LaBrecque *et al* 1996, Zhou and Dahlin 2003).

The LG array is a linear multi-electrode configuration which is a sort of 2D version of the resistivity grid (Cosentino *et al* 1999, Cosentino and Martorana 2003) that is a 3D array that works with hundreds of potential dipoles for each current injection.

The LG array (figure 3) has been designed in order to minimize the number of both current injections and electrodes used for current injection, but maintaining a resolution comparable to those of the more common arrays (i.e. W, DD, WS). For each current dipole, potential measurements are carried out for every adjacent electrode pair of the layout of the electrodes, both inside and outside the current dipole (in this way, the array is designed to fully exploit the multi-channel acquisition). The choice of number and positions of

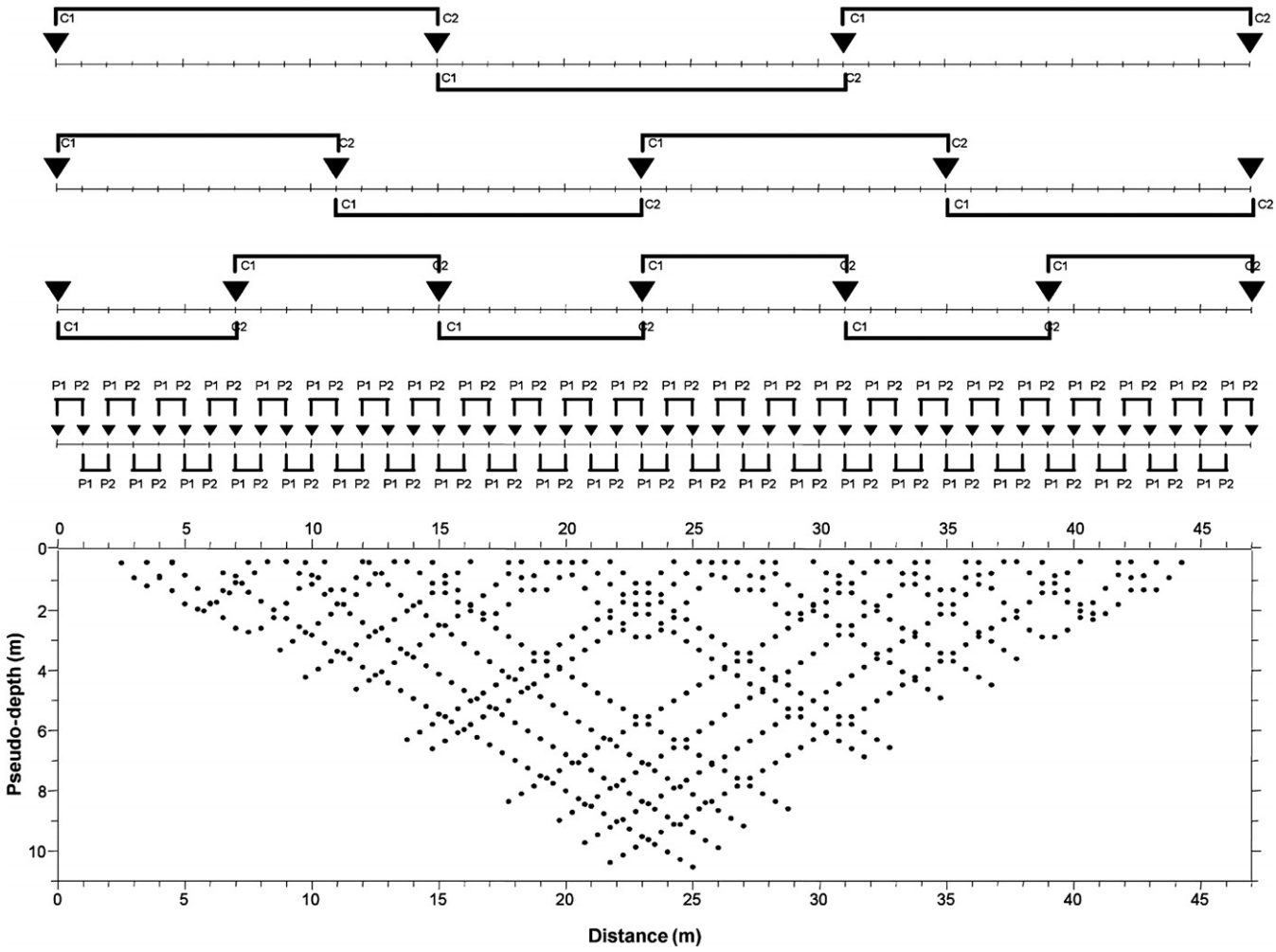

Figure 3. Sketch of the linear grid array. For each current dipole C1–C2, potential measurements are taken at each adjacent pair of electrodes P1–P2 (if the electrodes are not the same as the current electrodes). The reference points of the resulting pseudo-section are shown below

the current dipoles is determined by subdividing the electrode layout into equal parts and by locating the current electrodes at the ends of each part.

For our simulations with 48 electrodes, only 13 different current dipoles (in the buried-wall simulations) or 21 (in the sea intrusion-wedge simulations) were chosen, using two electrodes for current and the remaining 46 for potential.

The lengths of the current dipoles chosen for the buried-wall simulations were 1/6, 1/4 and 1/3 of the profile length; similarly, those for the intrusion simulations were 1/8, 1/6, 1/4 and 1/3. In this way, we used 13 current dipoles in the wall simulations (six dipoles having a length 1/6 of the profile length, four having a length of 1/4 and three having a length of 1/3) and 21 current dipoles in the sea intrusion simulations (the addition of eight current dipoles having a length of 1/8 of the profile was made to get a number of measurements comparable with those of the W, DD, WS arrays).

An interesting feature of the LG array (that will not be stressed in this paper) addresses the possibility of limiting errors caused by both contact resistances and polarization at electrodes (this last may well be referred to a fast exchange when employing the same electrode for current injection and potential measure). In fact, a limited number of current dipoles was used, compared with a large number of potential ones, thereby minimizing electrode polarization.

In place of a 'standard' resistivity meter, a representative instrument useful for the LG array is MRS-256 (GF Instruments): the current channel and the potential ones are completely separated in this instrument. In this way, the receiver records up to 256 quasi-contemporary potential measures for a single current injection. To summarize, the advantages of the combined use of the LG array and MRS256 are as follows.

(1) The multi-channel cables are strictly needed only for potential measurements, and the diameter of the cables can be very small because there is no significant current flow (light cables).

(2) The small number of electrodes used for current injection allows us to use dedicated electrodes for this purpose. In this way, there are no problems regarding electrode polarization. However, if dedicated electrodes for current injection are not used, the polarization is limited to the small number of current electrodes needed.

Table 2. Values of the electrode step, maximum order, number of measures and number of AB dipoles for each configuration used in the simulations

Array	Electrode step	Max. n factor	No of measures	No of AB dipoles
Buried-wall models, 48 electrodes, $a = 1$ m				
Wenner	$a \div 15a$		360	360
Wenner–Schlumberger	a	$n = 15$	465	465
Dipole–dipole	a	$n = 15$	570	45
Linear grid			565	13
Intrusion-wedge models, 48 electrodes, $a = 2$ m				
Wenner	$a \div 15a$		360	360
Wenner–Schlumberger	a, $2a$, $3a$	$n = 15$	854	707
Dipole–dipole	a, $2a$	$n = 15$	990	87
Linear grid			911	21

(3) The low number of current injections and the large number of quasi-contemporary potential measurements allow for fast acquisition of experimental data; the only time-consuming operations are electrode and cable deployment.

Fast acquisition of experimental data is also possible with a standard multi-channel resistivity meter, too, using all the available channels in contemporary acquisition. This characteristic is even more useful in the case of IP surveys.

Table 2 summarizes the electrode steps for each used array, the maximum value of the n factor, the number of simulated measures and the number of AB dipoles used for each simulation with both models. The maximum value of n for the DD and the WS arrays is 15 to enhance the resolution power of these arrays, even if the DD array provides a low signal-to-noise ratio.

We would further underline the fact that only a low number of current dipoles was necessary for the LG array in comparison to that of other arrays: this meant that a lot less time was needed to carry out the measurements.

4. Simulations

4.1. One buried wall

The first synthetic 2D model, depicted in figure 1(*a*), was designed to represent typical archaeological and engineering research. In fact, one of the problems most frequently met is recognizing wall structures of a size comparable to the electrode spacing, embedded at a shallow depth in a conductive overburden and lying on a resistive basement.

The model simulates a buried, highly resistive wall 50 cm wide and 1 m high, placed on a resistive basement and covered by a conductive layer. The resistivity values of the basement, the cover and the wall are 250 Ω × m, 40 Ω × m and 1200 Ω × m respectively. Therefore, the resistivity contrasts of the wall are equal to, respectively, 4.8 with respect to the basement and 30 with respect to the conductive overburden. The depth of the wall bottom is 1.5 m, while the thickness of the cover is 1.25 m. The 2D model was discretized with 5452 pixels (figure 1(*d*) shows the blocks near the wall). An array of 48 electrodes is placed over the model, with electrode spacing equal to 1 m. Note that the width of the wall is one-half that of the electrode spacing; therefore, this target should be difficult to detect with the electrode spacing chosen.

4.1.1. Pseudo-sections of apparent resistivity. The inversion program draws the initial computed pseudo-sections before proceeding with the inversions. Even though these are not, in principle, essential to the inversion of the resistivity data, the program does use some geometric parameters of the pseudo-sections in the inversion procedure. As a consequence, these parameters may be useful to the understanding of some of the features of the results obtained from the various configurations.

The apparent resistivity pseudo-sections calculated for the buried wall model are presented in figure 4. The data points are plotted at the median depth of investigation (following Edwards 1977). Even though the maximum n factor is the same ($n = 15$), the maximum pseudo-depth z_{max} is substantially different for each array. The thinnest pseudo-section was obtained with the DD array ($z_{max} \approx 3.5$ m) and the thickest one obtained was with the LG array ($z_{max} \approx 10.5$ m). Note that only the WS pseudo-section shows an anomaly that is easy to correlate with the buried wall geometry.

4.1.2. Inversion models. The various inverted models and the corresponding misfit images are presented in figure 5. The figure is divided into three boxes from top to bottom. The noise-free simulations are presented in the upper box, while the simulations of the middle and lower boxes were with data with noise added. Each of the three boxes shows the inversions obtained using the different investigated arrays (DD, W, WS, LG) in terms of inversion models (left) and the 2D distribution of the misfit parameter (right).

The models have only been plotted for the first 3 m, because below this depth there are no anomalies in the original model and all the tested arrays describe the resistivity of the basement quite well.

All the inverted models show the buried wall as an anomaly with a width at least double that of the synthetic model, due to the size of the inversion pixels (i.e. 1 m that is equal to the electrode spacing). All the arrays successfully identify both layers of the model (i.e. the resistive basement covered by the conductive overburden) quite well, but the inverted models are different. In particular, the main

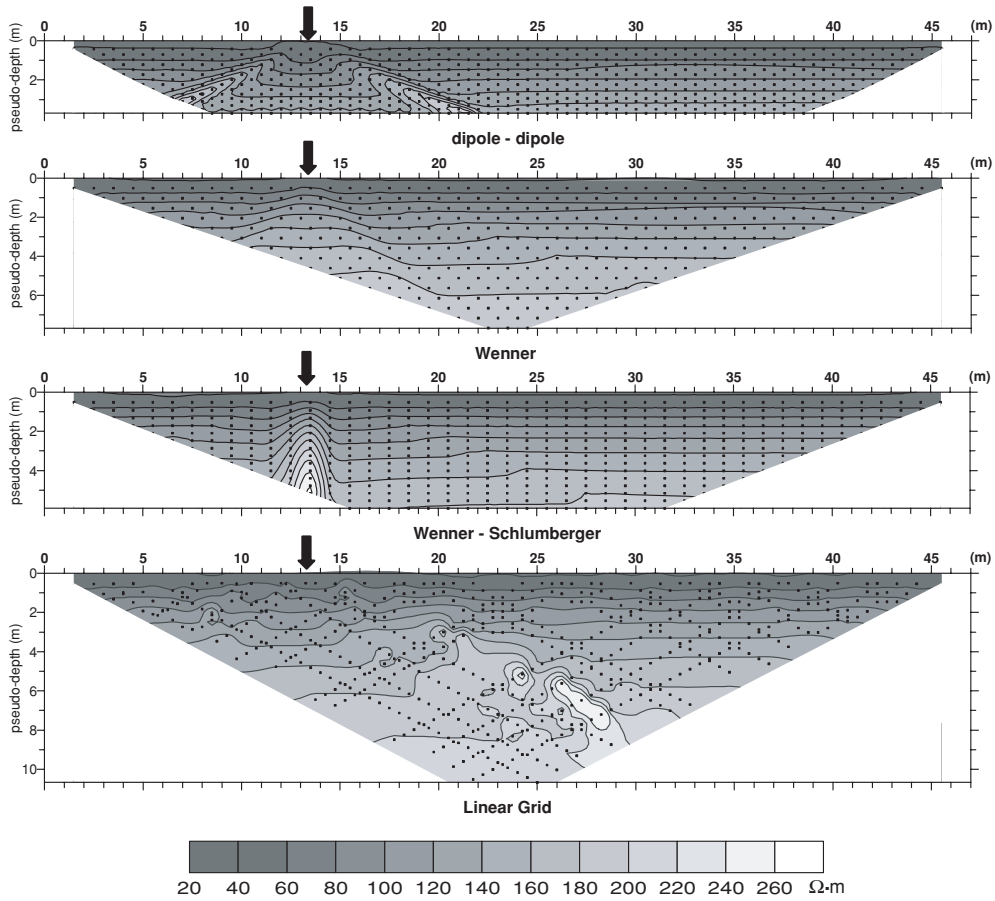

Figure 4. Calculated apparent resistivity pseudo-sections obtained by solving the forward problem of the model having one buried wall. The dots indicate the data positions used to plot each pseudo-section; the black arrows indicate the location of the buried wall on the *x*-axis.

differences are in the detection of the buried wall and the depth of the layers.

However, let us stress once more that only a few of the pixel boundaries of the inversion mesh coincide with the depths assigned to blocks in the synthetic models. For this reason, all the misfit images show, at the boundary between the overburden and the basement, a double layer composed of an upper overestimated resistivity and a lower underestimated one.

The DD array fits the resistivity of the buried wall (higher values) better, but the depth of the bottom of the wall is overestimated; there is a ghost anomaly on the right of the wall, which appears like a second less resistive vertical structure, and an underestimated resistivity area on the left of the wall, in the resistive basement.

The W array does not identify the wall as well as the DD array, in terms of both the resistivity value and the geometry, but there are no ghost anomalies. The pixel on the left of the wall, in the transition area between the layers, has a resistivity value close to that of the basement. Even though this is a better evaluation of the resistivity (see the misfit image), it complicates the recognition of the shape of the buried wall.

The WS array behaves qualitatively like the W array, but with a worse evaluation of the resistivity of both the wall and the basement.

The LG array gives very good results as far as the geometry of the entire model and wall is concerned, but the underestimation of the resistivity of the wall is greater than that obtained with the other arrays. The reason for this behaviour is clarified by the image of the misfit parameter: the resistive anomaly is spread beyond the boundaries of the wall. However, the resistivity contrast with regard to the surrounding pixels is high enough to recognize the wall as a sharp anomaly.

The corresponding results obtained using data with 2% of noise added are also presented in figure 5 (middle box). The addition of noise causes similar effects in all the arrays: a decrease in the resistivity of the anomaly corresponding to the wall and an increase in the misfit of the resistivity of both layers. Furthermore, the DD array gives many and more evident ghost anomalies, and the shape of the wall is less well defined. The LG array also presents anomalies that are not related to structures in the synthetic model, but that are definitely less intense than in the DD array.

Finally, figure 5 (lower box) shows the results obtained from the inversions of data with 5% of noise added. The DD array's inversion presents many resistive ghost anomalies (i.e. anomalies in the inverted models that do not correspond to any physical anomalies) inside the conductive layer. The resistivity of the wall is further diminished while the transition area between the layers near the wall has a resistivity value

closer to that of the wall. The WS array also presents resistive ghost anomalies in the conductive overburden, which are, however, less intense than those of the DD array. The wall recognition is the same as the data with 2% of noise added, but the lateral homogeneity of the boundary zone between the overburden and the basement decreases. In contrast, the W array does not recognize the upper part of the buried wall or the misfit in the resistive basement enhances. The LG array presents a lot of small ghost anomalies in the overburden and in the basement, but the wall is still clearly recognizable.

4.2. Two buried walls

This second 2D model (figure 1(*b*)) is similar to the first one but there are two buried walls in different positions from the first one. The wall in the central zone is like the first one in height, but is twice as wide (1 m). The wall on the left side is as large as the central one but is lower in height (62 cm). The depths of the bottom of the two walls are still 1.5 m. The resistivities and the thicknesses of the layers are equal to those of the previous model.

Pseudo-sections of apparent resistivity were also calculated for this model, but they were not very enlightening and unnecessary to data inversion; therefore, they have not been presented.

4.2.1. Inversion models. The various inverted models and the corresponding misfit images are presented in figure 6 in the same way as the previous model (i.e. in three boxes)

In this case, all the inverted models show two walls having a width equal to that of the single-wall model. In fact, the width of the walls in this model coincides with both the sampling rate and the lateral resolution. However, the positions of the wall boundaries coincide with the position of the electrodes, the detection of which is therefore optimal.

Furthermore, all the arrays identify the layers of the model quite well (within the above-mentioned limits) while the inverted models are different, particularly near the wall anomalies.

The DD and LG still appear to be the arrays that recognize the structures of this double-wall model better. As in the previous case, the noise level of 2% does not significantly disturb the detection of the structures, while an increase in noise to 5% gives a number of ghosts in all the inverted models, making it difficult to recognize the various parts of the model.

4.3. Three buried walls

The third 2D model (figure 1(*c*)) is essentially a combination of the first two models. That is, the background is the same as the previous ones while three anomalous walls are present, which have the same parameters as those contained in the first and second models.

The inverted models are presented in figure 7. The main observation to be made is that the DD array and LG array still appear to have the best geometrical resolving power, even though the values of the resistivity of the wall structures are not well retrieved. Furthermore, the results from the data with noise added are analogous to the previous ones, as can be inferred from the analysis of the central and lower boxes of figure 7.

Of interest in the figure is the fact that, when compared with the previous model inversions, you can observe the nonlinearity of the inverse problem; in other words, the addition of a wall, although not close to the other ones, deeply influences the inverted model.

4.4. Results obtained by varying the resistivity contrast and the depth of one buried wall

Starting from the model shown in figure 1(*a*), additional synthetic models were studied by decreasing the resistivity contrast of the buried wall with respect to the overburden and/or by increasing the depth of the wall and of the basement. The resistivity contrasts between the wall and the overburden used in the models were 30, 10 and 3 (resistivities of the wall equal respectively to 1200, 400 and 120 $\Omega \times$ m), while the depths of the wall bottom were 1.50, 1.75 and 2 m (then the thicknesses of the cover were 1.25, 1.5 and 1.75 m). The wall size (1 m high and 0.50 wide) is always the same. Noise of a 2% level was added to synthetic data.

Results of inversions and corresponding misfit images, for a restricted area of the model around the wall (5 m wide and 3 m thick), are shown in figure 8. The figure is subdivided into four boxes, one for each array. In each box the results obtained from the nine models, the resistivity of the wall decreasing from left to right and the depth of the wall increasing from top to bottom are presented. Inverted models are shown on the left and misfit images on the right.

The differences among the four tested arrays are confirmed even in these simulations: the DD array fits the resistivity of the buried wall better, while the LG array gives the best results in terms of geometry of the models. Using the other two arrays it is difficult to recognize the presence of the wall even with a cover thickness of 1.5 m, regardless of the resistivity contrast. In contrast, the LG and DD arrays do not recognize the wall for only two of the models (wall/cover contrast equal to 3 and cover thickness greater than 1.25 m).

4.5. Sea-intrusion wedge

The other synthetic model we selected represents salt-water intrusion in a coastal aquifer (figure 2). In this case, the lateral and vertical distributions of the resistivity are strongly determined by the pattern of the salt/fresh-water boundary. Thus, a good understanding of the resistivity model makes the reconstruction of the shape of the salt-water wedge in the aquifer possible.

The model simulates a sea-intrusion wedge (with a resistivity of 0.2 $\Omega \times$ m) in a coastal aquifer (resistivity equal to 80 $\Omega \times$ m) lying on a clay basement (2 $\Omega \times$ m). The 3.5 m thick aquifer is covered by a resistive overburden (150 $\Omega \times$ m) having a thickness of 1.5 m. The transition between salt water and fresh water is dipping (about 15%) and sharp. This model was discretized using 5452 blocks. Simulations were carried out with 48 electrodes, which were spaced at a distance of 2 m. The model is similar to that presented by Casas *et al* (2004).

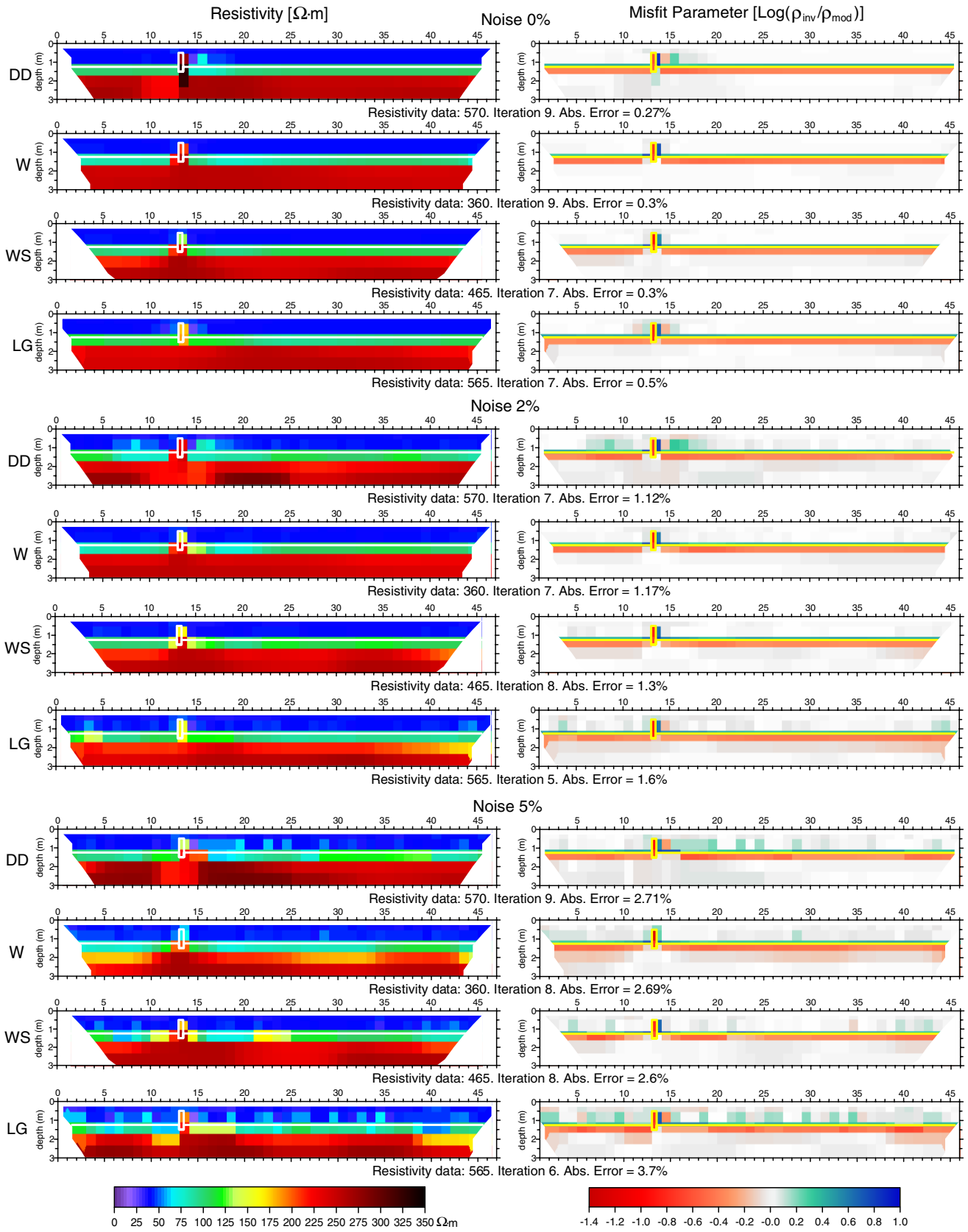

Figure 5. Interpretative models (on the left) and the corresponding misfit images (on the right) for the model with one buried wall. Simulations were carried out for the dipole–dipole array (DD), for the Wenner array (W), for the Wenner–Schlumberger array (WS) and for the linear grid array (LG). The results shown refer to noise-free data (top), 2% noise data (middle) and 5% noise data (bottom). White lines (left) and yellow lines (right) represent the boundaries of the synthetic model.

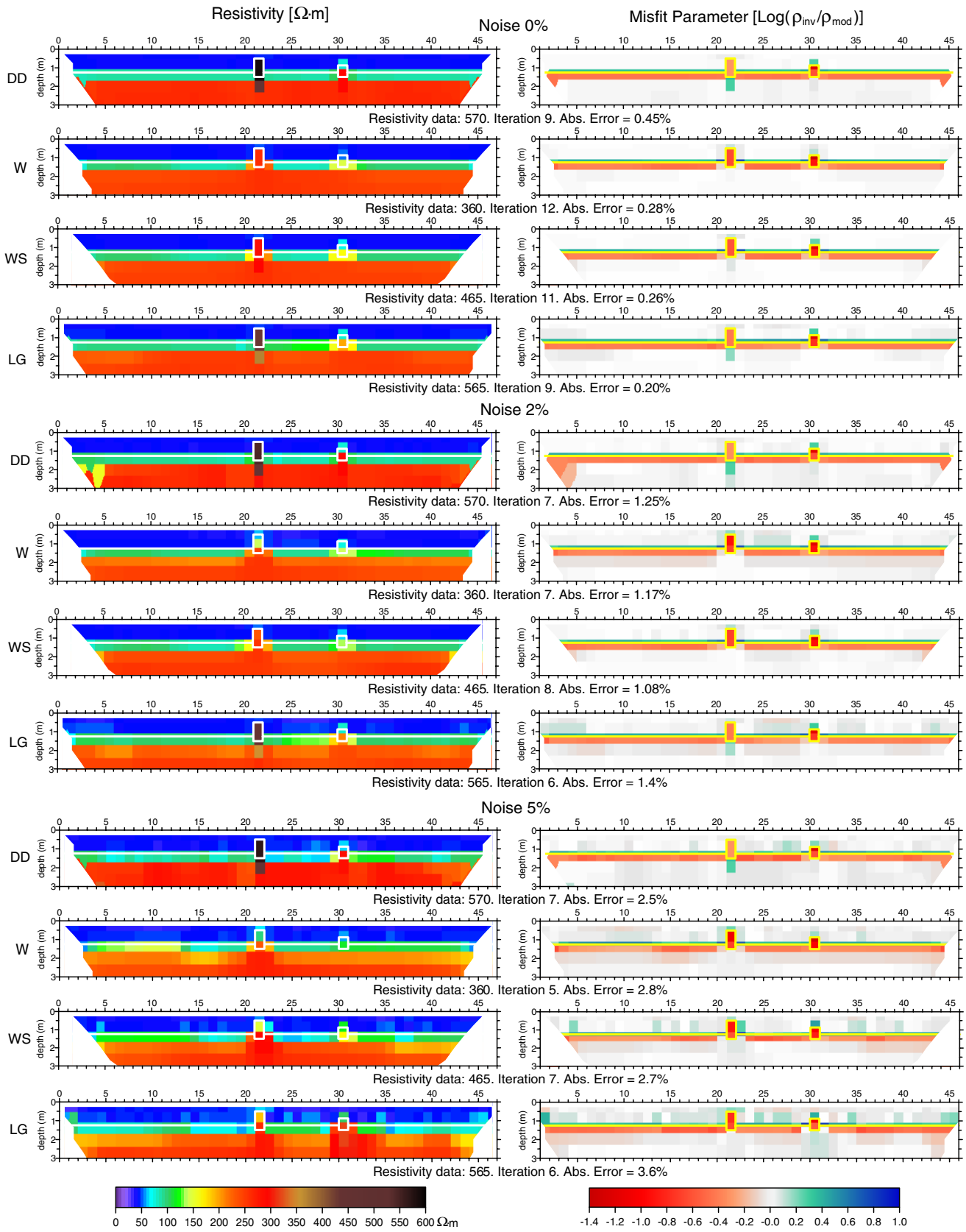

Figure 6. Interpretative models (on the left) and the corresponding misfit images (on the right) for the model with two buried walls. Simulations were carried out for the dipole–dipole array (DD), for the Wenner array (W), for the Wenner–Schlumberger array (WS) and for the linear grid array (LG). The results shown refer to noise-free data (top), 2% noise data (middle) and 5% noise data (bottom). White lines (left) and yellow lines (right) represent the boundaries of the synthetic model.

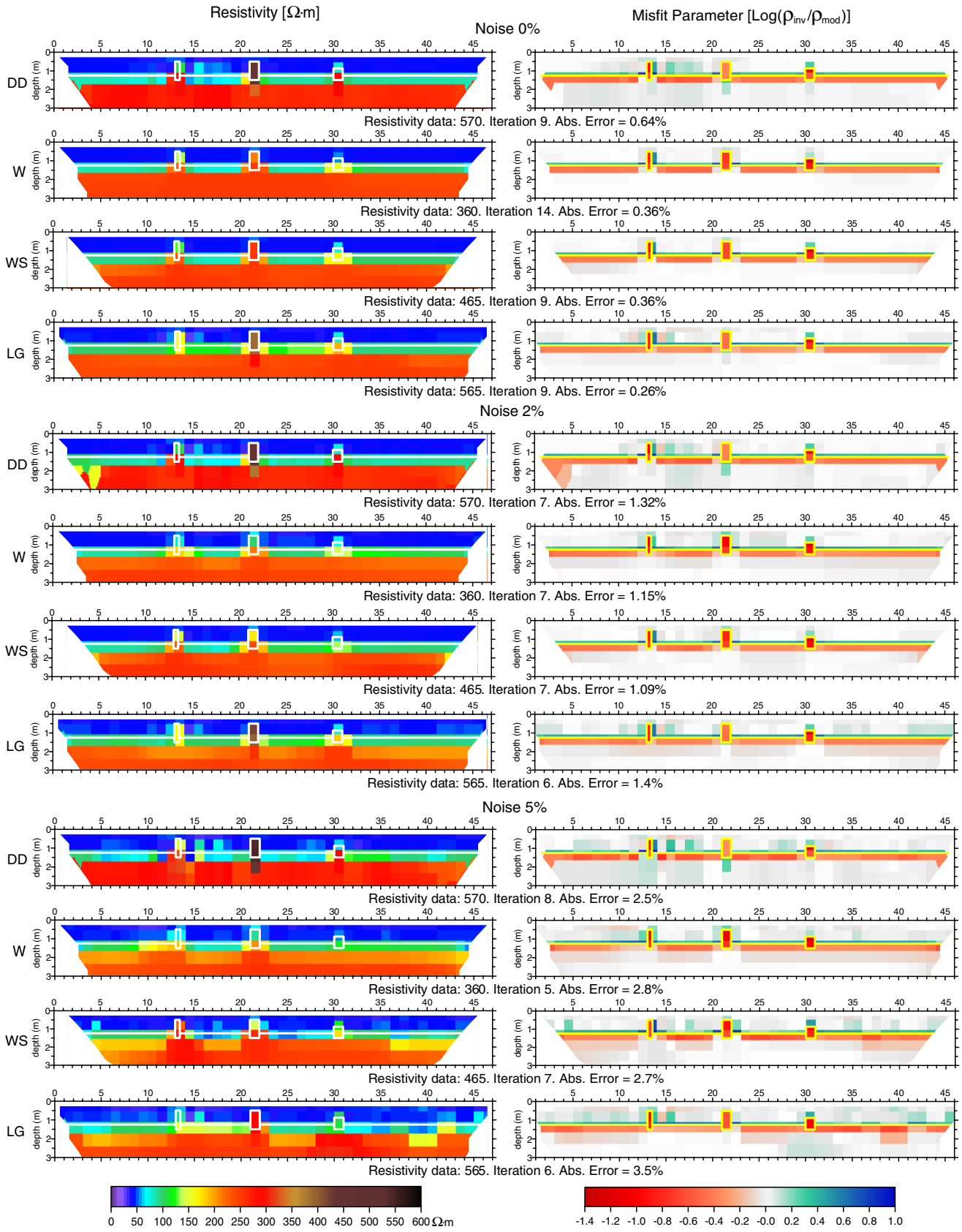

Figure 7. Interpretative models (on the left) and the corresponding misfit images (on the right) for the model with three buried walls. Simulations were carried out for the dipole–dipole array (DD), for the Wenner array (W), for the Wenner–Schlumberger array (WS) and for the linear grid array (LG). The results shown refer to noise-free data (top), 2% noise data (middle) and 5% noise data (bottom). White lines (left) and yellow lines (right) represent the boundaries of the synthetic model.

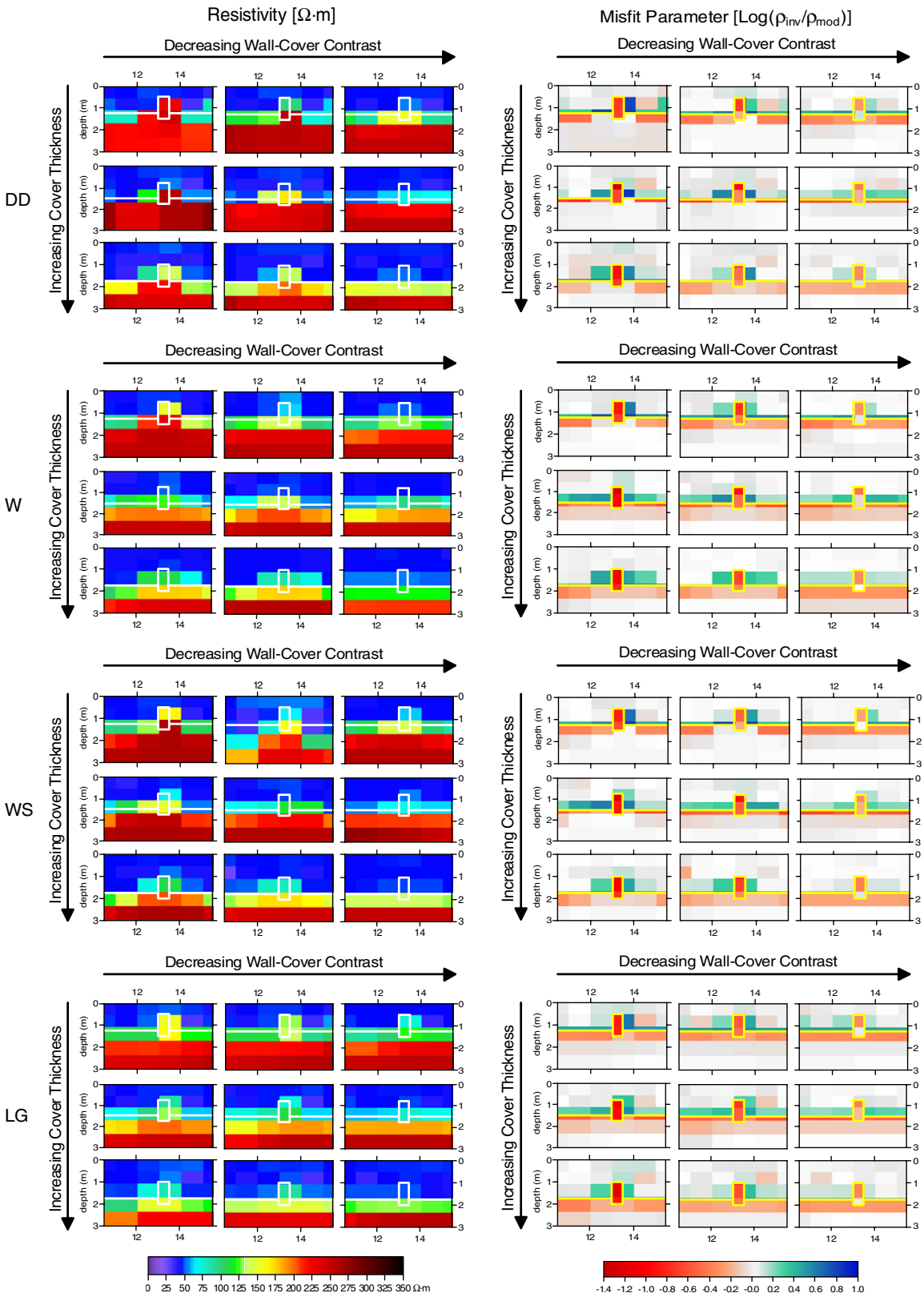

Figure 8. Inverted models (on the left) and corresponding misfit images (on the right) for models of one buried wall with varying resistivity contrasts and thicknesses of the cover. Simulations were carried out for the dipole–dipole array (DD), for the Wenner array (W), for the Wenner–Schlumberger array (WS) and for the linear grid array (LG). The results shown refer to 2% noise data. For each array the results of nine models are presented, grouped in a 3 × 3 matrix. In every row, the resistivity contrast between the wall and the cover decreases from left to right (respectively with values of 30, 10, 3), while in every column the thickness of the cover increases from top to bottom (respectively with values of 1.25, 1. 5, 1.75 m). White lines (left) and yellow lines (right) represent the boundaries of the synthetic models.

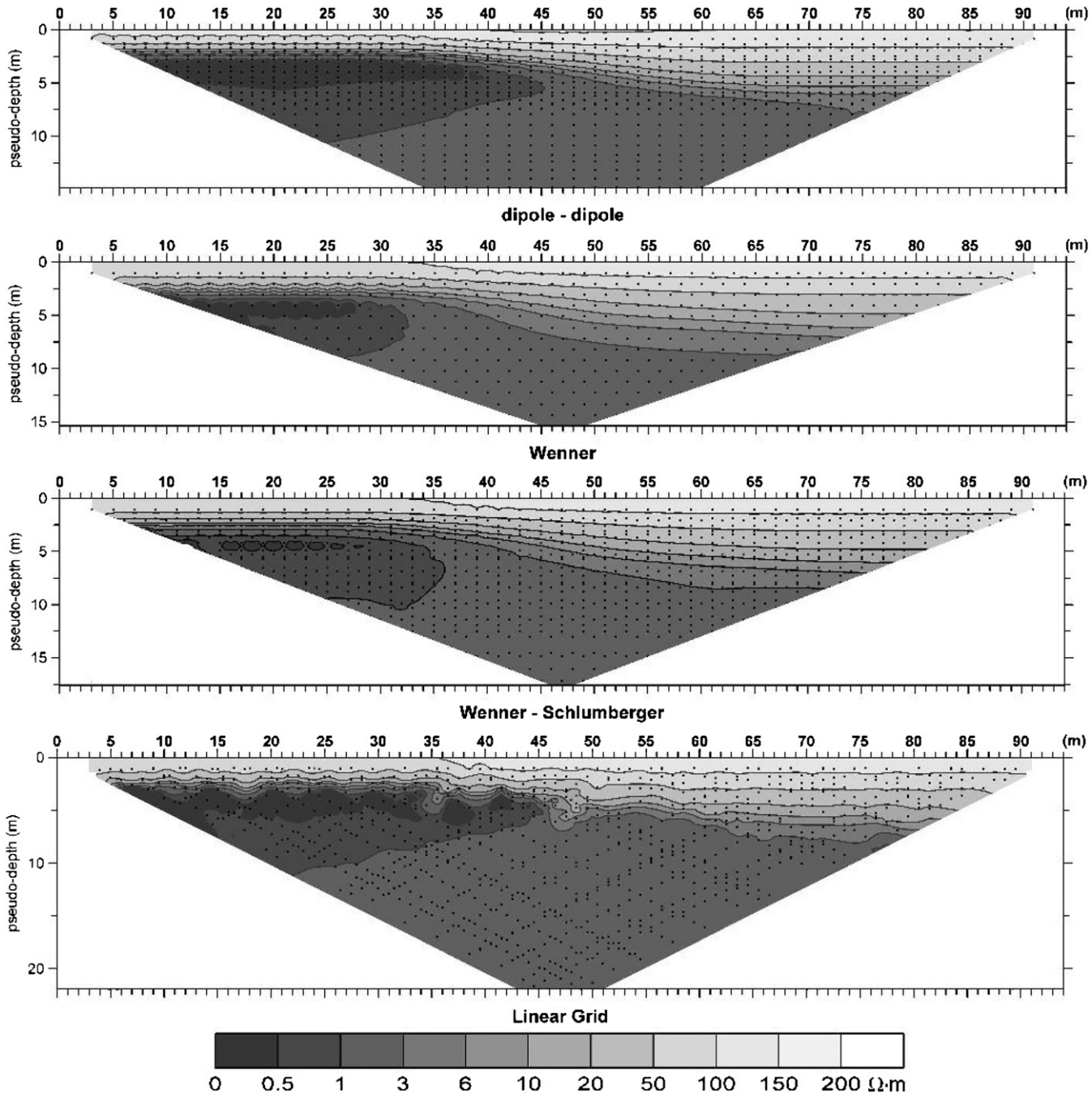

Figure 9. Calculated apparent resistivity pseudo-sections obtained by solving the forward problem of the sea-intrusion wedge model. The dots indicate the data positions used to plot each pseudo-section.

4.5.1. Pseudo-sections of apparent resistivity. The apparent resistivity pseudo-sections calculated for the aquifer model are presented in figure 9. For the DD and WS arrays, we used different electrode steps (see table 2) to investigate down to the clay basement. As a consequence of this choice, the number of measurements for these two arrays is higher than in the case of wall simulations. To compare arrays with similar numbers of measurements, another current dipole length was added to the LG array (current dipoles with the length equal to 1/8 of the profile). In the W-array, the highest number of measurements was used, compatible with a 48-electrode profile. However, as in the previous case, the maximum pseudo-depth z_{max} is substantially different for each array. The thinnest pseudo-section is for the DD array ($z_{max} \approx$ 15 m), while the deepest pseudo-section corresponds to the LG array ($z_{max} \approx$ 22 m). The W array and WS array pseudo-sections reach a maximum pseudo-depth of about 15.5 m and 17.5 m respectively.

4.5.2. Inversion model. As with the previous models, the various inversions and the corresponding misfit parameter images for the sea-water intrusion are presented in figure 10. Again, this figure has been divided into three boxes from top to bottom: the upper box presents the noise-free simulations

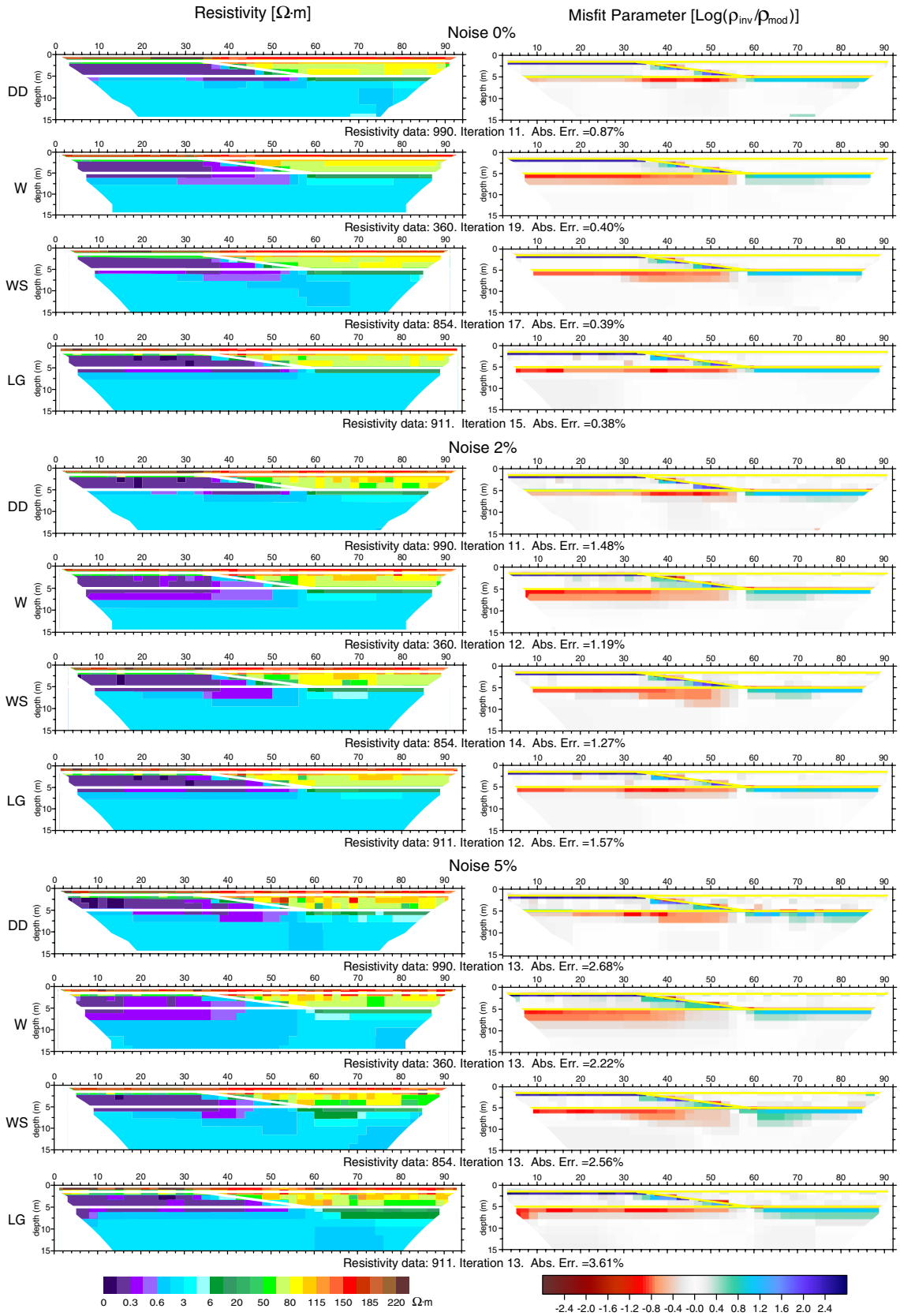

Figure 10. Interpretative models (on the left) and the corresponding misfit images (on the right) of the sea-intrusion wedge model. Simulations were carried out for the dipole–dipole array (DD), for the Wenner array (W), for the Wenner–Schlumberger array (WS) and for the linear grid array (LG). Results shown refer to noise-free data (top), 2% noise data (middle) and 5% noise data (bottom). White lines (left) and yellow lines (right) represent the boundaries of the synthetic model.

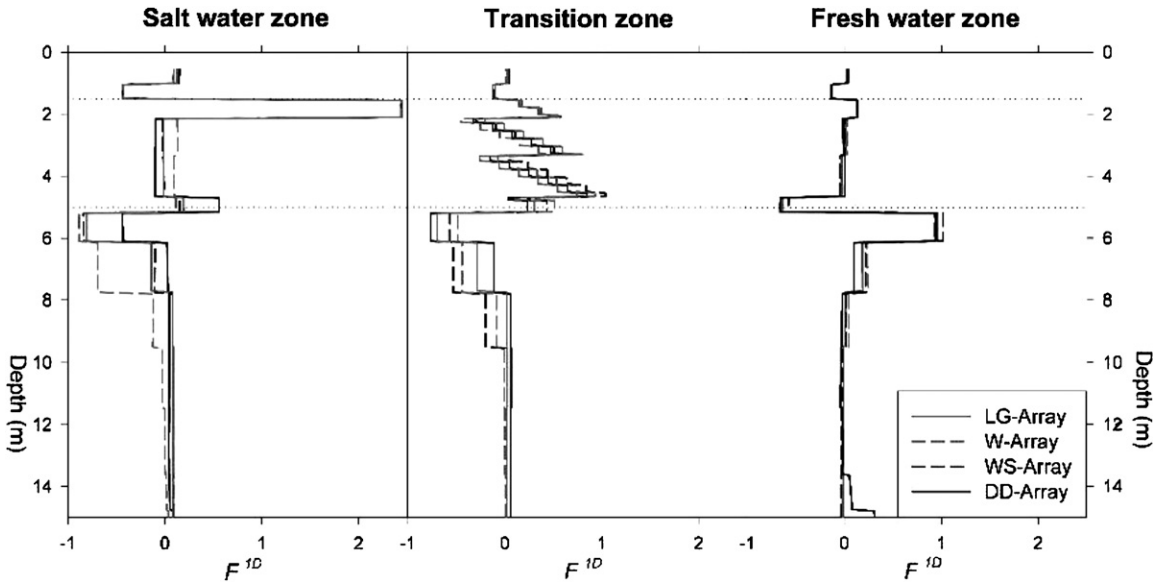

Figure 11. Plots of the 1D misfit parameter related to three different zones of the sea-intrusion wedge interpretative models. On the left, F^{1D} is calculated along the profile from $x = 0$ m to $x = 33$ m, in the middle from $x = 33$ m to $x = 59$ m and on the right from $x = 59$ to $x = 94$ m.

while the middle and lower boxes present the simulations with 2% and 5% noise respectively. As the spacing is double that of the previous models, these inverted models are deeper than those used to retrieve the buried walls, so that they are represented down to a depth of 15 m.

All the arrays identify the overburden, but they overestimate the value of the resistivity above the region intruded by the sea water. Neither in this case do the depths of the boundaries between the model layers correspond to the boundaries of the inversion pixels; consequently, the two horizontal transition zones that have different resistivities between the layers are unavoidable. The oblique transition zone between the sea wedge intrusion and the fresh-water aquifer is identified and well located in all the inversions of the tested arrays. Nevertheless, the results show differences, especially in the detection of the clay basement.

The W array and the WS array overestimate the depth to the clay layer under the intrusion wedge more than the other arrays. This behaviour is shown both in the inversion images and more clearly in the misfit images. In these latter images, the red zones under the intrusion wedge highlight an underestimation of resistivity. In the WS inversions, the underestimation of resistivity is not uniform under the intrusion wedge, but it is more pronounced when it is in a position equivalent to that of the transition zone.

The DD array and the LG array better recognize the boundaries of the zones having different resistivities, the main discrepancies being connected to the misfit between the boundaries of the inversion blocks and the model blocks.

Figure 10 (middle and bottom) shows inversions obtained from simulations on the sea-intrusion wedge with the addition of random Gaussian noise (σ equal to 2% and 5% of the apparent resistivity). In this model, noise has a smaller effect than in the wall models. In fact, the features of the inversions (obtained by all the tested arrays) remain similar to simulations from data without noise, regardless of the noise level. This is probably due to the larger lateral dimensions of the investigated structures.

The 1D misfit parameter, referred to 2% noise simulations, is presented in figure 11, which is divided into three sections respectively regarding three different portions of the profile: the salt-water area, the transition zone and the fresh-water area.

In the salt-water area, the W array gives worse results in recognizing the basement than the other arrays. Furthermore, there are slight differences at depths between 2 m and 4.7 m, with small over- or underestimations of the resistivity values. In positions corresponding to inversion layers that include contacts between the aquifer and clay, the DD array gives resistivity values close to the value of the upper layer, while the other arrays give values close to that of the lower one.

Even in the transition zone, the main discrepancies occur in the clay zone, with best results for the DD array, respectively, followed by LG, W and WS arrays, while all the arrays adequately recognize the fresh-water zone.

Similar simulations were also done on models of sea-intrusion wedges with smooth transitions between salt- and fresh-water aquifers (obtained using a number of oblique layers of gradually varying resistivities). The results obtained were equivalent to those presented above so that they are not shown here.

5. Tests on experimental data

The comparison between DD and LG arrays was also extended to two field cases. Obviously, in the field cases the comparison between the inversion model and the 'true' model is generally impossible. For this reason, we chose to investigate a site with very consistent *a priori* information.

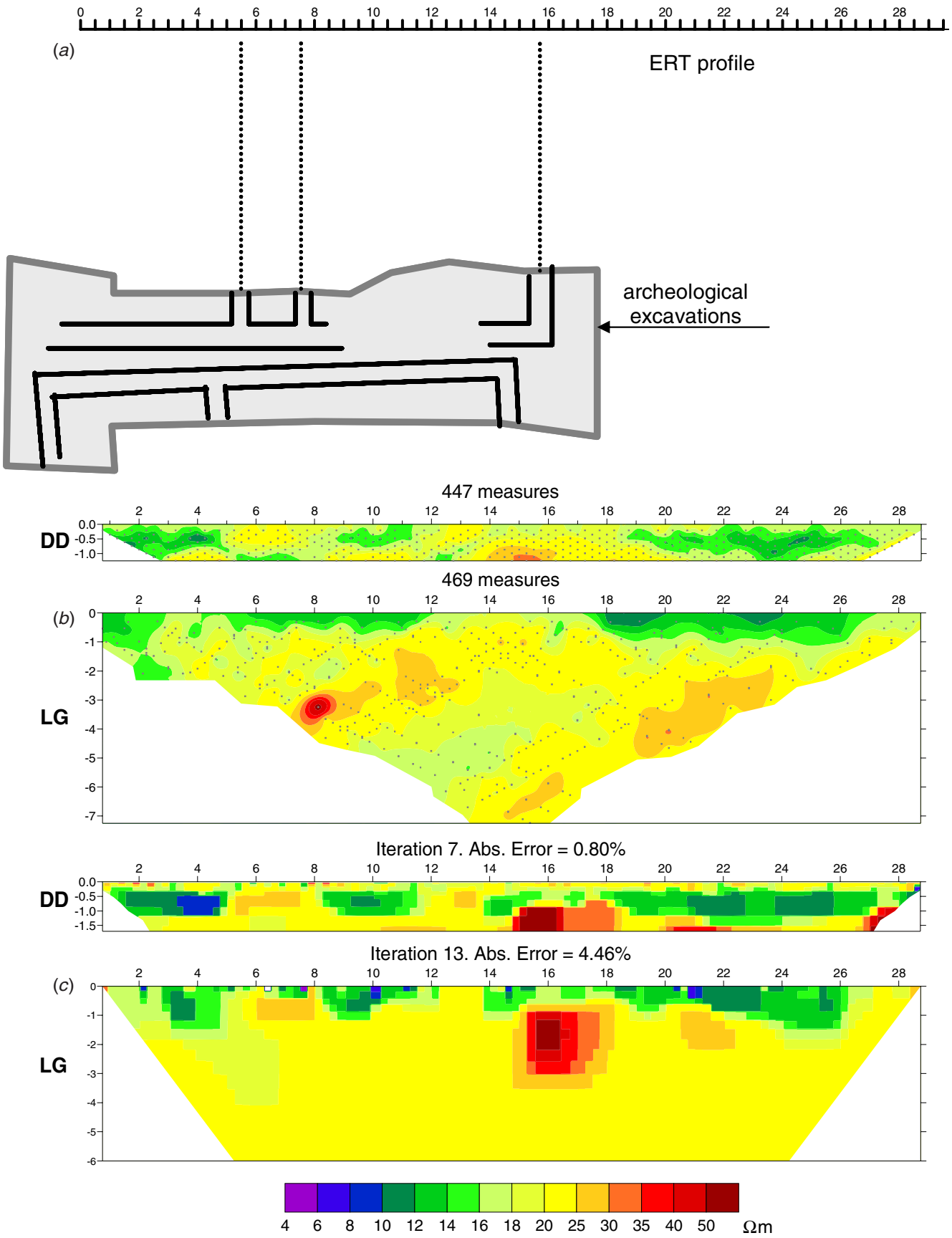

Figure 12. Results of a geoelectrical survey carried out in the archaeological site of Himera (Italy) by using DD and LG arrays: (*a*) Map of the profile and of the archaeological excavations (the dotted lines indicate the presumed elongations of the walls), (*b*) apparent resistivity pseudo-sections and (*c*) interpretative models.

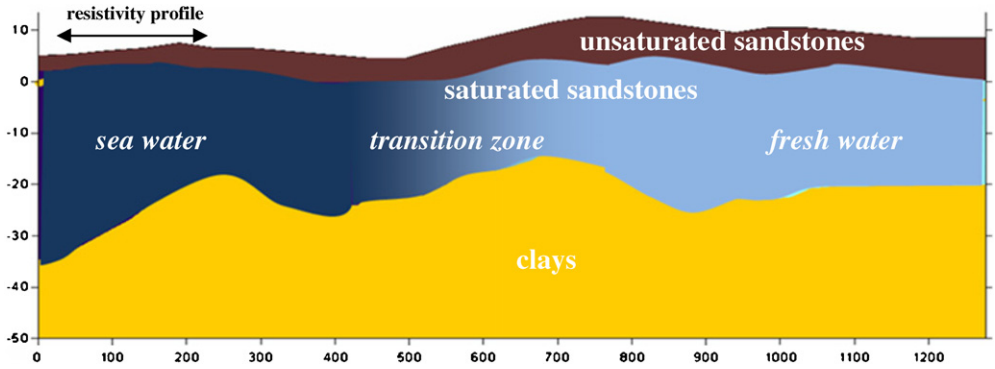

Figure 13. Schematic hydrogeological section of the coastal aquifer between Marsala and Mazara del Vallo (Italy). The arrowed line indicates the position and the extent of the electrical tomography.

5.1. Buried walls

This geoelectrical investigation is part of a geophysical survey carried out at the Himera archaeological site, where relics of a Greek settlement are still buried (Capizzi *et al* 2007). The relics are the remains of ancient buildings (sandstone walls and floors) buried in alluvional clays transported by the floods of the Himera river. The survey was performed over buried walls partially exposed by a previous excavation (figure 12(*a*)) The profile direction was perpendicular to the buried walls found during the excavation activities, to verify the continuity of these structures.

The 2D resistivity survey was performed using 64 electrodes at 0.5 m spacing (figure 12(*b*)). Due to the high noise level, the measurements of the DD array were carried out up to $n = 9$ (instead of $n = 15$ as in the simulations), for a total of 513 measurements (61 different current dipoles). ARES G4 (GF Instruments) was used to perform the measurements.

The LG array survey was made using the same 64 electrodes for potential measurements, while 9 additional current electrodes were used for current injection. In this way, it was possible to utilize a MRS-256 instrument with the above-mentioned advantages. 13 different current dipoles were used (three dipoles with a length of 1/3, four dipoles with a length of 1/4 and six dipoles with a length 1/6 of the whole profile) for a total number of 819 measurements.

A direct comparison of the survey time between DD and LG cannot be done because different resistivity meters were used, but we can consider that, typically, a multi-channel resistivity meter takes about 20 s to carry out all the measurements related to the same current injection (with ten repetitions for each datum). In this field case for the DD array, an acquisition sequence of about 20 min would be necessary, while for the LG array only about 4 min is needed. Half an hour is generally needed to drive the electrodes into the ground and to connect the cables. Thus, using the LG array can save about 30% of the required time.

Data sets were inverted by using RES2DINV software with the previously described parameters (table 1).

The models obtained by data inversion (figure 12(*c*)) show resistive anomalies having shapes well correlated with the assumed archaeological structures. In fact, the suspected perimeter wall continuations intersect the resistivity profile consistent with the resistive anomalies, whose depths also agree with those detected by excavations. The DD-array inversion model shows higher resistivity contrasts than the LG array, but it implies a smaller investigation depth (this is because we used only one step in the DD array). Furthermore, it is also possible to recognize the base of the main wall in the LG-array inversion model.

5.2. Sea-intrusion wedge

Resistivity measurements were acquired during an extended study of the coastal aquifer located in South-Western Sicily, between the towns of Marsala and Mazara del Vallo (Cosentino *et al* 2007). A huge sea-intrusion wedge extends up to about 600 m from the coastal line. A comparison between DD, WS and LG arrays was performed in the first 200 m of the intruded area, where the intrusion phenomenon is more manifest. Preliminary information about the resistivity distribution in the subsoil was provided by previous geophysical, geochemical, hydrological and geological studies. Up to the investigation depth reached by the resistivity profile, the subsoil is essentially sandstone (the clay basement of the aquifer is deeper than 30 m), so the resistivity variations are mainly due to the salinity of the water contained. This zone is completely sea-water intruded, with a conductivity greater than 5000 μS cm^{-1} (the total extent of sea-water intrusion was detected at about 500–600 m from the coastal line). A schematic hydrogeological section of this area is shown in figure 13.

The survey was performed using a Syscal Pro resistivity meter, equipped with two cables, each with 24 take-outs (spaced 2 m). The roll-along technique was used to reach a whole profile length of 190 m. For each 48-electrode profile section, and for each array, the sequence of data acquisition was the same as described in the above-presented simulations.

For this survey, using a ten-channel resistivity meter, which is able to carry out contemporaneously all the measurements with the same current injection, 10 h is necessary for the WS-array acquisition sequence (because the WS array is performed using one channel at a time), 1 h for the DD-array acquisition sequence, while only 13 min is needed for the LG array. Considering 1 h to deploy the electrode array,

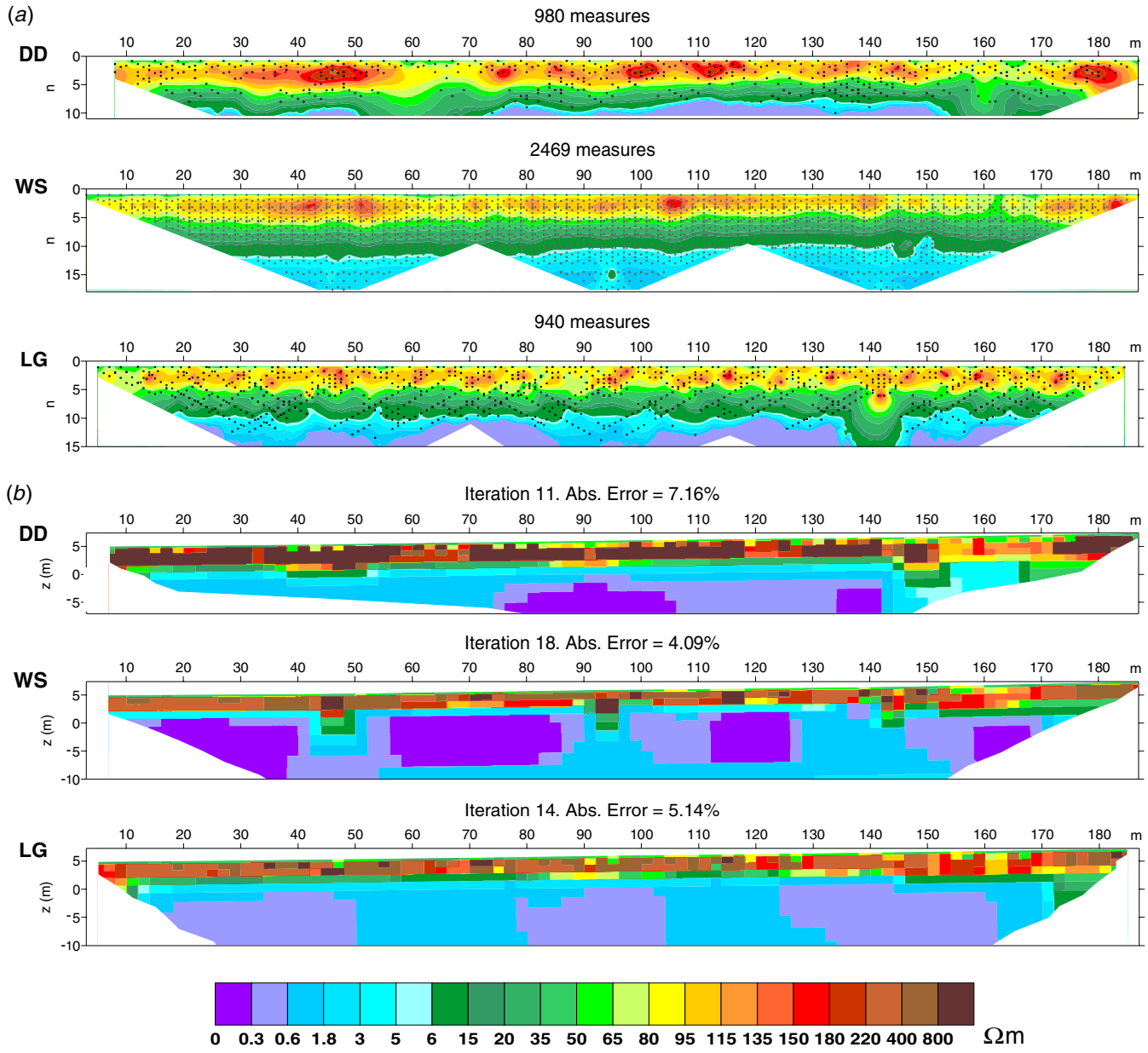

Figure 14. Geoelectrical survey carried out to study the sea-intrusion wedge in a coastal aquifer of South-Western Sicily, between the towns of Marsala and Mazara del Vallo (Italy). Comparison of DD, WS and LG arrays: (*a*) apparent resistivity pseudo-sections and (*b*) interpretative models.

to connect and roll along the cables, in this case using the LG array can imply about 40% of time saving in comparison with the DD array and 90% in comparison with the WS array.

Measurements with a standard deviation greater than 10% were rejected before the data were inverted. Mainly for the DD array data set, this caused the rejection of several data at a high pseudo-depth, which are very noisy, because of the high geometric factors and very low resistivity values (figure 14(*a*)). All data sets were inverted by using RES2DINV software with the previously described parameters (table 1). The interpretation of the geoelectrical data was done by comparing the results with those obtained from other geophysical surveys (seismic, transient electromagnetic, induced polarization), as well as drilling surveys and geological information (Cosentino *et al* 2007). The various models obtained by the inversion procedure show the same strong variation of resistivity with depth (figure 14(*b*)). This vertical change has been interpreted as the transition from nonsaturated to saturated sandstones, as confirmed by water-table measurements carried out at nearby water wells. In the near-surface zone a heterogeneous resistive level is present, and its pattern is consistent in the inversion models obtained with different arrays. Due to the rejection of highly noisy data, the DD-array inversion model reaches a shallower depth than the others. The saturated zone in the LG-array model is more uniform than in the WS-array model, in which some lateral variations appear corresponding to of the areas of the pseudo-section with limited data.

6. Conclusions

It is very difficult to evaluate discrepancies between interpretative and synthetic models, by only looking at the colour image of the resistivity models, even though the adopted colour scale is highly detailed. In fact, in this case the image reading would be very complicated. Therefore, the 2D misfit parameter images, combined with the resistivity images, allow for the zone-by-zone quantitative estimation of the discrepancies. In some cases, especially for vertical discrepancies, the 1D misfit parameter can give simple quantitative estimates of the fit quality.

The proposed models are (especially those with a buried wall) sensitive to the spacing of the electrodes and the pixel mesh selected for the inversion. Consequently, we cannot expect satisfactory results when the noise level is high. In practice, a compromise should be made to take into account the geometrical resolution, the geometry of the investigated structures and the noise level, in such a way as to assure the reliability of the results. These considerations are challenging when the *a priori* knowledge of the model is limited, in particular as regards the sharpness or smoothness of the resistivity gradients at the boundaries between the different parts of the model.

On the whole, from our simulations and field tests, we can say the following.

(1) When the structures are large in comparison with resolution, the arrays respond well with regard to the resistivity values, with small differences (among the arrays) regarding the shapes and boundaries of the investigated structures.
(2) When the investigated structures are small in comparison with resolution, the responses can favour the recovery of either the shapes and boundaries of the structures or the resistivity values. The latter can only be of advantage if real values of resistivity and not the resistivity contrast are desired: in this case, for resistive anomalies, the DD array seems to give better results.

For each tested array the main features, in terms of advantages and limits, are summarized below.

6.1. DD array

Inversions of the DD array data fit the geometry of the structures quite well and, in the buried wall simulations, they fit the real resistivity of the wall better.

If a DD array is used with only one electrode step (equal to the electrode spacing), the investigation depth is shallower than that given by the other arrays. Instead of increasing the dipole n factor (with a consequent decrease in the signal level) we used two electrode steps for the sea-intrusion wedge model, which lead to approximately double the number of measurements (990 instead of 570).

The number of current dipoles in the DD array is low compared with the W array and WS array. In fact, in theory, it is possible to perform all measurements for each current injection simultaneously, thereby reducing the acquisition time.

6.2. W array

The W array gives the worse results for the sea-intrusion wedge models. In fact, the depth of the top of the clay basement is overestimated. Only the models with shallower walls are interpreted quite well, even though the shape of the wall is not clearly recognized.

The number of apparent resistivity measurements for the W array is the lowest among the tested arrays, but this feature does not imply smaller acquisition times when using a multi-channel resistivity meter, because of the high number of current dipoles used. Therefore it is not indicated, in terms of acquisition time, with a multi-channel acquisition system.

6.3. WS array

The results of the buried-wall WS-array models are similar to those obtained using the W array. On the other hand, the inversion obtained for the WS array intrusion model determined a lower boundary of the clay zone under the transition zone.

One electrode step is not sufficient to explore deep structures; therefore, three electrode steps were used in the sea intrusion WS-array model simulations. Therefore, the number of measurements was greatly increased. In all the tested models, a large number of current dipoles was used.

6.4. LG array

The LG array recognizes the shapes of the investigated structures in wall and seawater intrusion models quite well. Inversions do not present significant ghost anomalies. The LG-array sea intrusion-wedge model, like the DD-array model, clearly recognizes the contact between the clay basement and the aquifer. The LG array exhibits the best quality in terms of pattern recognition of the investigated structures.

Furthermore, the LG-array data sets were obtained using only 13 current dipoles for the wall simulations and 21 for the intrusion-wedge ones. The choice of increasing the number of current dipoles (and consequently the number of measurements) was made to compare the resolution power of the LG array with DD and WS arrays using about the same number of data. However, even with 13 current dipoles, the quality of the LG array inversions is better than that of the W array, and the investigation depth remains greater than the other models.

These features show that the LG array can be very useful especially when using a multi-channel acquisition system because of the decreased acquisition time. In fact, considering a hypothetical 48-channel resistivity meter and an acquisition time for each multi-channel measurement of the order of several seconds, a few minutes can be sufficient to complete an acquisition with 48 electrodes, instead of the several tens of minutes needed using the 'classical' arrays.

The study of the behaviour of a new array on two different classes of models is not sufficient to establish the capability of this array to recognize structures and resistivity contrasts on different models, even though the classes of models chosen are representative of a wide range of field situations. Simulations

of additional models are necessary to adequately characterize the LG array's properties well and they are still in progress. Preliminary results using both experimental and synthetic, data seem to confirm many useful characteristics of the LG array.

References

Capizzi P, Cosentino P L, Fiandaca G, Martorana R, Messina P and Vassallo S 2007 Geophysical investigations at the Himera archaeological site, northern Sicily *Near Surf. Geophys.* **5** 417–26

Casas A, Himi M, Tapias J C, Ranieri G and Mota R 2004 Mapping salt water intrusion in coastal aquifers by electrical imaging using different arrays: a comparative study *Proc. 18th SWIM (Cartagena, Spain)*

Cosentino P, Capizzi P, Fiandaca G, Martorana R, Messina P and Pellerito S 2007 Study and monitoring of salt water intrusion in the coastal area between Mazara del Vallo and Marsala (South-Western Sicily) *Methods and Tools for Drought Analysis and Management* (*Series: Water Science and Technology Library* vol 62) (Berlin: Springer) pp 303–20

Cosentino P and Martorana R 2003 High-resolution micro-geophysics: electrical tomography for walls *Proc. 3rd Asamblea Hispano Portuguesa de Geodesia y Geofísica, (Valencia, Spain)* pp 1794–8

Cosentino P, Martorana R and Terranova L M 1999 The resistivity grid to optimize tomographic 3D imaging *Proc. 5th Meeting of EAEG, European Section (Budapest, Hungary)* Em12

Dahlin T 1996 2D resistivity surveying for environmental and engineering applications *First Break* **14** 275–83

Dahlin T and Loke MH 1998 Resolution of 2D Wenner resistivity imaging as assessed by numerical modelling *J. Appl. Geophys.* **38** 237–49

Dahlin T and Zhou B 2004 A numerical comparison of 2D resistivity imaging with 10 electrode arrays *Geophys. Prospect.* **52** 379–98

Daily W and Owen E 1991 Crosshole resistivity tomography *Geophysics* **56** 1228–35

Deidda G P, Ranieri G, Uras G, Cosentino P and Martorana R 2006 Geophysical investigations in the Flumendosa River Delta, Sardinia (Italy). Seismic reflection imaging *Geophysics* **71** B121–8

Edwards L S 1977 A modified pseudosection for resistivity and induced polarization *Geophysics* **42** 1020–36

Fiandaca G, Martorana R and Cosentino P L 2005 Use of the linear grid array in 2D resistivity tomography *Proc. Near Surface 2005—11th European Meeting of Environmental and Engineering Geophysics (Palermo)* A023 4 pp

Goldman M, Gilad D, Ronen A and Melloul A 1991 Mapping of sea water intrusion into the coastal aquifer of Israel by the time domain electromagnetic method *Geoexploration* **28** 153–74

Hagemeyer R T and Stewart M 1990 Resistivity investigation of salt-water intrusion near a major sea-level canal *Geotechnical and Environmental Geophysics* (*SEG Book Mart, Academic Series* vol 2) ed S H Ward pp 67–77

Hoekstra P and Blohm M V 1990 Case histories of time-domain electromagnetic soundings in environmental geophysics *Geotechnical and Environmental Geophysics* (*SEG Book Mart, Academic Series* vol 2) ed S H Ward pp 1–15

Khesin B E 1969 *Mining Geophysics in Mountainous Regions* (Moscow: Nedra) (in Russian)

Khesin B 2001 Induced polarization method as a tool for the study of seawater invasion into coastal aquifer *Enviromental Engineering and Composite Materials* (*Scientific Israel—Technological Advantages* vol 3) pp 12–9

Khesin B, Alexeyev V and Eppelbaum L 1996 *Interpretation of Geophysical Fields in Complicated Environments* (*Bookseries: Modern Approaches in Geophysics* vol 14) (Berlin: Springer) p 352

LaBrecque D, Miletto M, Daily W, Ramirez A and Owen E 1996 The effects of 'Occam' inversion of resistivity tomography data *Geophysics* **61** 538–48

Li Y G and Oldenburg D W 1992 Approximate inverse mapping in DC resistivity problems *Int. Geophys. J.* **109** 343–62

Loke M H 2002 RES2DMOD ver. 3.01—rapid 2D resistivity forward modelling using the finite-difference and finite-element methods *Freeware*© 28 pp

Loke M H and Barker R D 1995 Least-squares deconvolution of apparent resistivity pseudosections *Geophysics* **60** 1682–90

Loke M H and Barker R D 1996 Rapid least-squares inversion of apparent resistivity pseudosections by a quasi-Newton method *Geophys. Prospect.* **44** 131–52

Mills T, Hoekstra P, Blohm M and Evans L 1988 Time-domain electromagnetic soundings for mapping sea water intrusion in Monterey County, CA *Ground Water* **26** 771–82

Olayinka A and Yaramanci U 2000 Assessment of the reliability of 2D inversion of apparent resistivity data *Geophys. Prospect.* **48** 293–316

Oldenburg D W and Li Y G 1999 Estimating depth of investigation in dc resistivity and IP surveys *Geophysics* **64** 403–16

Park S K and Van G P 1991 Inversion of pole–pole data for 3-D resistivity structure beneath arrays of electrodes *Geophysics* **56** 951–60

Patra H P 1967 A note on the possibility of saline-water invasion around the Jadha coast, West Bengal (India) *Geoexploration* **5** 95–101

Sasaki Y 1992 Resolution of resistivity tomography inferred from numerical simulation *Geophys. Prospect.* **40** 453–63

Sasaki Y 1994 3-D resistivity inversion using the finite-element method *Geophysics* **59** 1839–48

Shima H 1992 2-D and 3-D resistivity imaging reconstruction using crosshole data *Geophysics* **55** 682–94

Stewart A P 1982 Evaluation of electromagnetic methods for rapid mapping of salt-water interfaces in coastal aquifers *Ground Water* **20** 538–45

Storz H, Storz W and Jacobs F 2000 Electrical resistivity tomography to investigate geological structures of the Earth's upper crust *Geophys. Prospect.* **48** 455–71

Van G P, Park S K and Hamilton P 1991 Monitoring leaks from storage ponds using resistivity methods *Geophysics* **56** 1267–70

Veshev AV 1965 *Electric Profiling by Direct and Alternating Currents* (Moscow: Nedra) (in Russian)

Yang C-H, Tong L-H and Huang C-F 1999 Combined application of dc and TEM to sea-water intrusion mapping *Geophysics* **64** 417–25

Zhou B and Dahlin T 2003 Properties and effects of measurement errors on 2D resistivity imaging *Near Surf. Geophys.* **1** 105–17